Probing magnetic anisotropy and spin-reorientation transition in the three-dimensional antiferromagnet Ho₀.₅Dy₀.₅FeO₃|Pt using spin Hall magnetoresistance

Aditya A. Wagh [1,*] Priyanka Garg [1,†] Arijit Haldar [1,2] Kingshuk Mallick,[1] Tirthankar Chakraborty,[1] Suja Elizabeth,[1] and P. S. Anil Kumar [1,‡]

¹Department of Physics, Indian Institute of Science, Bangalore, INDIA
²Department of Physics, University of Toronto, 60 St. George Street, Toronto, Ontario, M5S 1A7 Canada

Orthoferrites (RFeO₃) containing rare-earth (R) elements are 3D antiferromagnets (AFMs) that exhibit characteristic weak ferromagnetism originating due to slight canting of the spin moments and display a rich variety of spin-reorientation transitions in the magnetic field (H)-temperature (T) parameter space. We present spin Hall magnetoresistance (SMR) studies on a b plate (ac plane) of crystalline Ho₀.₅Dy₀.₅FeO₃|Pt hybrid at various T in the range 11–300 K. In the room temperature Γ_4 phase, the switching between two degenerate domains occurs at fields above a critical value, $H_c \approx 713$ Oe. Under $H > H_c$, the angular dependence of SMR (α scan) yielded a highly skewed curve with a sharp change (sign-reversal) along with a rotational hysteresis around the a axis. Notably, at $H < H_c$, the α-scan measurements on the single degenerate domain exhibited an anomalous sinusoidal signal of periodicity 360°. Low-T evolution of the SMR curves ($H = 2.4$ kOe) suggests weakening of the anisotropy possibly due to the T evolution of Fe-R exchange coupling. Below 25 K, the SMR modulation showed an abrupt change around the c axis, marking the presence of a Γ_2 phase. We have employed a simple Hamiltonian and computed SMR to examine the observed skewed SMR modulation. In summary, SMR is found to be an effective tool to probe magnetic anisotropy as well as a spin reorientation in Ho₀.₅Dy₀.₅FeO₃. Our spin-transport study highlights the potential of Ho₀.₅Dy₀.₅FeO₃ for future AFM spintronic devices.

I. INTRODUCTION

Antiferromagnetic (AFM) insulators are envisaged as the next-generation memory devices to exploit switching of the Néel vector [1–5]. They offer advantages over ferromagnets (FMs), such as zero macroscopic magnetization, enhanced robustness against magnetic field (H) fluctuations, and faster switching dynamics [6–8]. In recent years, the potential of AFM passive layers has been highlighted in various spintronic devices [9–12]. For instance, in the experimental demonstration of a magnon valve, a passive insertion layer of AFM NiO was used to weaken magnetostatic coupling between the two adjacent Y₃Fe₅O₁₂ (YIG) layers while allowing the magnon transport [13]. On the other hand, the passive AFM layers are found to play a key role in pinning the adjacent FM layers in some spintronic devices [14]. Moreover, exotic spin configurations in AFMs have been seen to absorb spin currents at AFM-heavy metal (HM) interfaces resulting in interesting modulations in spin Hall magnetoresistance (SMR) [15–17]. AFMs are observed to exhibit characteristic negative SMR (out-of-phase modulation) compared to the conventional positive SMR in collinear FMs [18–26]. Recent studies on FM|AFM|HM have highlighted the high tunability of (nonlocal) SMR signals in such devices [14,27–29]. 3D AFM materials exhibit very rich magnetic phase diagrams [30–34]

and, hence, are a good prospect for studying spin-transport phenomena. Further, SMR at the AFM-HM interface can be a useful probe to investigate various magnetic phases and phase transitions in 3D AFMs.

SMR studies on epitaxial thin film SmFeO₃|Ta bilayers showed that the sign of the SMR was positive and an ordering of the Sm sublattice enhanced its magnitude at low temperatures [35]. In another investigation on epitaxial film, TmFeO₃|Pt, the SMR was particularly measured in the transversal geometry [spin Hall-induced anomalous Hall effect (SHAHE)] to probe the spin reorientation transition (SRT) [36] from a Γ_4 to Γ_2 phase [37] (representations are in Bertaut's notation [38]). In a recent report on the single-crystal hybrid DyFeO₃|Pt, the angular dependence of SMR in the Γ_4 phase was examined, while rotating the $\boldsymbol{H}$ in the ab plane. The observed sharp anomalies in SMR were analyzed using a simple phenomenological model and attributed to the sudden change in the Néel vector [39].

In DyFeO₃, the Fe sublattice undergoes an SRT, $\Gamma_4 \xrightarrow{50\,\mathrm{K}} \Gamma_1$, whereas HoFeO₃ exhibits $\Gamma_4 \xrightarrow{58\,\mathrm{K}} \Gamma_{412} \xrightarrow{50\,\mathrm{K}} \Gamma_2$ with an intermediate transition region, Γ_{412} [40–42]. Alternatively, some neutron studies on single-crystal HoFeO₃ claimed that there are two SRTs; $\Gamma_4 \xrightarrow{55\,\mathrm{K}} \Gamma_1 \xrightarrow{36\,\mathrm{K}} \Gamma_2$ [43]. Chakraborty and Elizabeth [44] reported the presence of twofold SRT, in their magnetic studies on single crystals of Ho₀.₅Dy₀.₅FeO₃, i.e., $\Gamma_4 \xrightarrow{50\,\mathrm{K}} \Gamma_1 \xrightarrow{26\,\mathrm{K}} \Gamma_2$. In the present paper, we investigate spin transport at the single crystal Ho₀.₅Dy₀.₅FeO₃|Pt interface. We examined the twofold SRT in Ho₀.₅Dy₀.₅FeO₃ using SMR as our measurement probe.
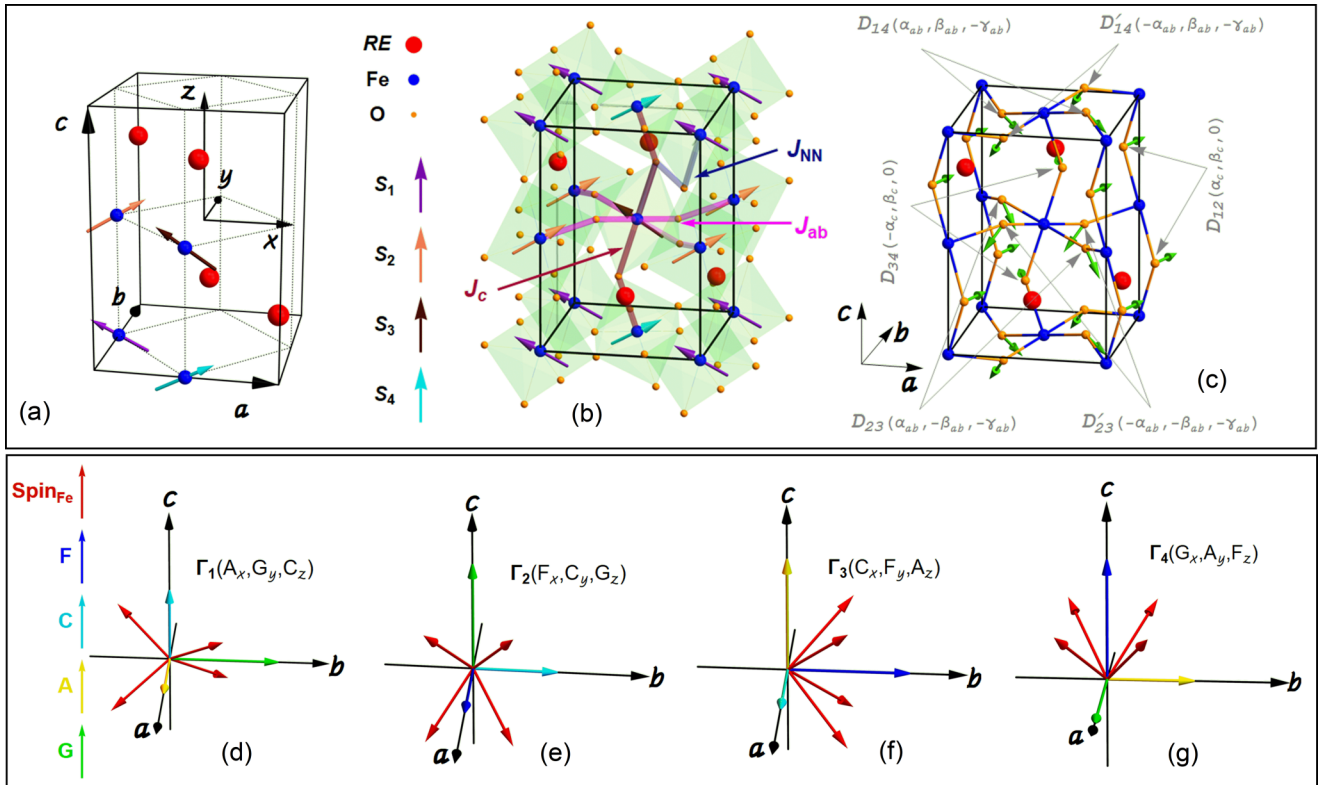
*adityawagh@iisc.ac.in
†priyankagarg@iisc.ac.in
‡anil@iisc.ac.in

FIG. 1. Magnetic unit cell of perovskite orthoferrite, $RFeO_3$. (a) Orthorhombic unit cell with lattice vectors, $\boldsymbol{a}$, $\boldsymbol{b}$, and $\boldsymbol{c}$. Four Fe^{3+} spin moments are located at special positions. (b) Two types of exchange interactions between Fe^{3+} spin moments: (1) nearest neighbor interaction (J_{ab} and J_c) and (2) next-nearest neighbor interaction (J_{NN}). (c) Various Dzyaloshinskii-Moriya vectors are represented with green arrows. (d)–(g) Different representations of *Pbnm* space group such as Γ_1, Γ_2, Γ_3, and Γ_4 along with Fe^{3+} spin moments and their respective basis vectors ($\boldsymbol{F}$, $\boldsymbol{C}$, $\boldsymbol{A}$, and $\boldsymbol{G}$).

In the Γ_4 phase at room temperature (RT), both basis vectors $\boldsymbol{G}_{Fe}$ (the Néel vector) and $\boldsymbol{F}_{Fe}$ (weak ferromagnetism) lie in the *ac* plane. Therefore, we chose a *b* plate of $Ho_{0.5}Dy_{0.5}FeO_3$ single crystal and studied angular dependence of SMR while rotating the $\boldsymbol{H}$ in the *ac* plane. Our choice of the plane for $\boldsymbol{H}$ rotation, which is different from that of the *ab* plane in a recent report on $DyFeO_3$, yielded some interesting results [39]. Angle-dependent SMR modulation revealed a sharp anomaly near the *a* axis which was notably accompanied by a rotational hysteresis. To investigate the SMR, we employed a simple model considering competing interactions acted upon Fe spins that include the nearest-neighbor and the next-nearest-neighbor exchange, Dzyaloshinskii-Moriya (DM) interaction, anisotropy and Zeeman energy. Notably, additional paramagnetic contribution from rare-earth sublattice [45] was essential to account for the observed magnetization and SMR.

In the Γ_4 phase, a degeneracy of Fe-spin configuration (or domains), characterized by $\Gamma_4(+G_x, +F_z)$ and $\Gamma_4(-G_x, -F_z)$ (refer to Appendix A for the phase representations), allows achieving a single domain of the choice by applying H above a critical value (H_c). Our low-field ($H < H_c$) SMR measurements on such single domains yielded a signal with anomalous periodicity of 360° compared to the typical periodicity of 180° in conventional SMR signals. Next, we trace the SRTs $\Gamma_4 \xrightarrow{49\,K} \Gamma_1 \xrightarrow{26\,K} \Gamma_2$ by carrying out SMR measurements at

low temperatures. In the Γ_4 phase at lower temperatures, an overall reduction in the skewness of the SMR modulation was observed. This points toward the weakening of the anisotropy and can have possible origin in the presence of Fe-R exchange coupling and its temperature evolution. In this paper, we have discussed in detail the effectiveness of SMR as a tool to examine magnetic anisotropy as well as spin reorientation in 3D AFM, $Ho_{0.5}Dy_{0.5}FeO_3$.

II. MAGNETIC PHASES AND SPIN REORIENTATION IN $HO_{0.5}DY_{0.5}FEO_3$

Orthoferrite $Ho_{0.5}Dy_{0.5}FeO_3$ exhibits a distorted perovskite crystal structure with orthorhombic space group *Pbnm* ($a = 5.292$, $b = 5.591$, and $c = 7.614$) [44]. Figure 1(a) represents such an orthorhombic unit cell with lattice vectors, $\boldsymbol{a}$, $\boldsymbol{b}$, and $\boldsymbol{c}$. A pseudocubic perovskite cell is shown with dashed lines for reference. The orthorhombic unit cell consists of four Ho^{3+}/Dy^{3+}, four Fe^{3+}, and twelve O^{2-} ions. Magnetic ions (Ho^{3+}/Dy^{3+} and Fe^{3+}) sit at the inequivalent positions as shown in Fig. 1(a) [46]. Among Fe^{3+} and Ho^{3+}/Dy^{3+} magnetic sublattices, the former sublattice comprises of $\boldsymbol{S}_1, \boldsymbol{S}_2, \boldsymbol{S}_3, \boldsymbol{S}_4$ spin moments and is represented by four arrows of distinct colors. Notably, an alternative system (xyz) is also shown in which $\boldsymbol{x}$, $\boldsymbol{y}$, and $\boldsymbol{z}$ are parallel to $\boldsymbol{a}$, $\boldsymbol{b}$, and $\boldsymbol{c}$, respectively.

In a typical orthoferrite, magnetism is complex due to various competing superexchange interactions such as intra-sublattice interactions (denoted by constants J^{Fe-Fe} and J^{R-R}) and intersublattice interactions (denoted by constant J^{Fe-R}). Generally, Fe-sublattice orders at high temperature ($T_N^{Fe} >$ RT) and hence J^{Fe-Fe} interactions are prominent. Similarly, R-sublattice orders at very low temperature ($T_N^R < 10$ K) and consequently, J^{R-R} interactions play an important role at these low temperatures. However, the R sublattice is known to contribute to magnetism above T_N^R via weak J^{Fe-R} interactions. In $Ho_{0.5}Dy_{0.5}FeO_3$, Fe-sublattice orders antiferromagnetically at high temperatures much above 400 K and J^{Fe-Fe} interactions mainly account for the AFM in it [44]. R-sublattice ordering in $HoFeO_3$ and $DyFeO_3$ systems has been reported to be below 10 K [39,41]. Our present study on $Ho_{0.5}Dy_{0.5}FeO_3$ was carried out at temperatures higher than 10 K hence, J^{Fe-Fe} are dominant interactions and discussed in detail. Distortions in the ideal perovskite unit cells result in distinct exchange interaction constants for the two nearest-neighbor Fe spin interactions; in-plane (ab plane), J_{ab}, and between the planes (c direction), J_c [see Fig. 1(b)]. Similarly, the next-nearest-neighbor exchange interaction between Fe spins is crucial [47] and is represented by the constant J_{NN} [see Fig. 1(b)].

Cooperative distortions in the unit cell result in displacement of oxygen ions and further lead to DM interactions between the respective Fe spins. The DM interactions coupled with exchange interactions manifest in canting of Fe spins. Various DM interactions are denoted by respective DM vectors (D_{14}, D'_{14}, D_{23}, D'_{23}, D_{34}, and D_{12}) with green arrows in Fig. 1(c) [47].

In 3D AFMs such as orthoferrites, phase transformations among $\Gamma_1(A_x, G_y, C_z)$, $\Gamma_2(F_x, C_y, G_z)$, $\Gamma_3(C_x, F_y, A_z)$, and $\Gamma_4(G_x, A_y, F_z)$ phases [see Figs. 1(d)–1(g)] are commonly observed under the influence of temperature or magnetic field. (The magnetic phase representations are illustrated in Appendix A). Such transformations involve continuous (second-order transition) or abrupt (first-order transition) rotation of certain basis vectors and hence they are popularly known as SRTs. In the present case of $Ho_{0.5}Dy_{0.5}FeO_3$, AFM order sets at high temperature well above 400 K and $\Gamma_4(G_x, A_y, F_z)$ phase stabilizes. Even as the temperature is lowered, the $\Gamma_4(G_x, A_y, F_z)$ phase persists down to $T_{SR1} = 49$ K and then abruptly transforms to the $\Gamma_1(A_x, G_y, C_z)$ phase [44]. Further, around $T_{SR2} = 26$ K, another transformation to the $\Gamma_2(F_x, C_y, G_z)$ phase has been reported [44]. Notably, under the application of magnetic field along the c axis, the $\Gamma_1(A_x, G_y, C_z)$ phase was seen to transform to the $\Gamma_4(G_x, A_y, F_z)$ phase. The critical field required for this first-order transition increases with decreasing temperature [44]. It is apt to compare these phases with those in the parent orthoferrites, $HoFeO_3$ and $DyFeO_3$ [40,41,43]. In $HoFeO_3$, phase transitions occur in the following order as the temperature decreases: $\Gamma_4 \xrightarrow{T_1} \Gamma_{412} \xrightarrow{T_2} \Gamma_2 \xrightarrow{T_3}$, antiferromagnetically ordered Ho phase, while in $DyFeO_3$ the following sequence is reported: $\Gamma_4 \xrightarrow{T_1} \Gamma_1 \xrightarrow{T_2} \Gamma_5$ (antiferromagnetically ordered Dy phase). A recent report, with the help of spin transport studies, has shown that Dy spin moments get ordered due to the exchange interactions with Fe spins in the temperature range, T_N^{Dy} to 23 K [39]. We emphasize that the magnetic
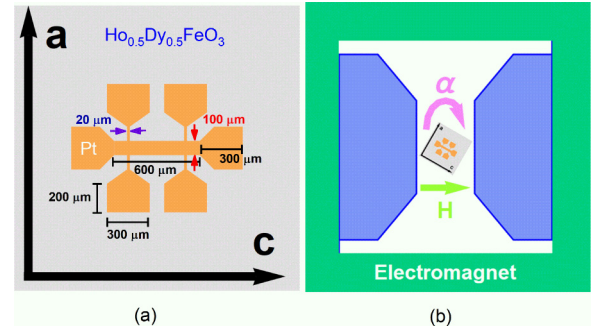

FIG. 2. Schematic of spin Hall magnetoresistance measurement: (a) Pt-Hall bar patterned on ac plate of single crystal of $Ho_{0.5}Dy_{0.5}FeO_3$, (b) SMR device mounted on a rotating probe inside electromagnet (top view). Uniform constant magnetic field is applied in the plane of the device.

phase diagram of $Ho_{0.5}Dy_{0.5}FeO_3$ at low temperature is rich due to SRTs, the related hystereses and a complex interplay between Fe and R sublattices.

III. EXPERIMENTAL DETAILS

Single crystal $Ho_{0.5}Dy_{0.5}FeO_3$ was grown by optical floating-zone method [44]. The crystal was oriented using back-reflection Laue technique and cut into a rectangular-shaped ac plate. The plate was polished with diamond paste (particle size ≈ 0.25 μm) and the roughness of the surface was estimated using AFM as $R_{rms.} \approx 2$ nm. A platinum (Pt) layer of 5 nm thickness was deposited on the polished surface of an ac plate by electron beam evaporation. Next, a Pt Hall bar was patterned using optical lithography which was followed by argon ion beam etching [refer to Fig. 2(a) for dimensions and orientation of the Hall bar]. For the RT SMR measurements, the sample was mounted on a custom-built rotating probe, which is incorporated with a Lakeshore electromagnet (2 T) [see Fig. 2(b)]. Angular dependence of SMR was measured while rotating the sample in clockwise (α scan) and counter-clockwise ($-\alpha$ scan) manner at various constant H values in the range 350 Oe to 16 kOe. Here, an ac current (333 Hz) of amplitude, $I_{P-P} = 2$ mA, was applied using Keithley 6221 DC/AC Current Source and the transverse voltage signal was measured with a Stanford Research SR830 lock-in amplifier. For low-temperature SMR studies (down to 11 K), the device was mounted on a modified closed-cycle refrigerator equipped with rotating magnet arrangement (2400 Oe) and the transverse voltage was measured by passing $I_{P-P} = 1$ mA.

IV. MODEL OF SPIN HALL MAGNETORESISTANCE

This section describes a simple model to compute SMR in $Ho_{0.5}Dy_{0.5}FeO_3$ single crystal. To compute SMR, we first estimate the equilibrium magnetic moment configuration of the magnetic unit cell. At high temperatures, $Ho_{0.5}Dy_{0.5}FeO_3$ exhibits a Γ_4 magnetic phase in which the interactions between the Fe spins are dominant. It is to be noted that R ordering occurs below 10 K and R-Fe interactions have been observed to persist and affect spin transport in a $DyFeO_3$ system up to 23 K [39]. Therefore, we make a simple assumption that

R spin ordering is absent in the high-temperature Γ_4 phase. However, the paramagnetic moment of the *R* sublattice can contribute to the total magnetization of the unit cell as it is influenced by both external magnetic field (**H**) and local fields induced due to the ordering of the Fe sublattice.

The equilibrium spin moment configuration of the Fe sublattice was estimated by minimizing the effective Hamiltonian $\mathcal{H}$ with respect to Fe spin moment components: S_i^x, S_i^y, and S_i^z ($i = 1$ to 4). Here, $\mathcal{H}$ comprises different competing interactions acted upon Fe spins, such as exchange, anisotropy, Zeeman, and DM interactions. These interactions and related constants used in the minimization calculations are elaborated on in Appendix B. Subsequently, *R* moments S_k ($k = 5$ to 8) are determined considering their paramagnetic alignment (at high temperature) under the combined influence of **H** and the net moment of the Fe sublattice (**F**), i.e., $\mu_0(\mathbf{H} + \mathbf{F})$.

In $Ho_{0.5}Dy_{0.5}FeO_3$ single crystal, we are studying angular dependence of transverse SMR by rotating **H** in the *ac* plane. We employ a simple model of SMR for FMs that is described in the literature [20,21]. This model has been used in a variety of complex magnetic phases such as collinear, canted, and spiral AFMs because the magnetic unit cell is typically much smaller than the spin diffusion length of electrons in the adjacent platinum layer. According to this model, the transverse resistivity ($\rho_{\text{sim}}^{\text{SMR trans}}$) for applied **H** in the *ac* plane can be given as,

$$\rho_{\text{sim}}^{\text{SMR trans}} = \Delta\rho_1 \langle S_i^x S_i^z \rangle + \Delta\rho_2 S_i^y + \Delta\rho_{\text{Hall}} H_b,$$
$$\text{where} \quad i = 1 \text{ to } 8. \tag{1}$$

Here, the first term is transverse SMR, the second term represents SHAHE and the last one is due to the ordinary Hall effect (OHE). $\Delta\rho_1$ and $\Delta\rho_2$ are resistivities that are proportional to the real part (G_r) and the imaginary part (G_i) of the spin-mixing conductance, respectively. Notably, the SHAHE term depends on out-of-plane (OOP) components (along *b* axis) of the spin moments, i.e., S_i^y. The OHE is governed by the Hall resistivity, $\Delta\rho_{\text{Hall}}$, and OOP component of the **H**, i.e., H_b.

V. RESULTS AND DISCUSSION

A. Room-temperature magnetization

In the absence of **H** at RT, the Γ_4 phase is the stable phase in $Ho_{0.5}Dy_{0.5}FeO_3$ [44]. Figure 3 shows magnetization (*M*)-field (*H*) isotherms $M_{c\,\text{exp}}$ and $M_{a\,\text{exp}}$, measured while scanning the **H** in the range, -17 to 17 kOe at RT along *c* and *a* axes, respectively. The inset shows a magnified view of $M_{c\,\text{exp}}$ versus **H** curve highlighting a sharp switching accompanied by a hysteresis. The critical field (H_c) required for the switching between $\Gamma_4(+G_x, +F_z)$ and $\Gamma_4(-G_x, -F_z)$ domains is estimated to be ≈ 713 Oe. To understand experimentally measured *M-H* curves along *c* and *a* axes at RT, we simulated the equilibrium magnetization by minimizing $\mathcal{H}$ in Eq. (B2b). We realized that the simulated magnetization considering the Fe sublattice alone $M_{c\,\text{sim}}^{\text{Fe}}$ ($M_{a\,\text{sim}}^{\text{Fe}}$) cannot account for the experimentally measured magnetizations, $M_{c\,\text{exp}}$ ($M_{a\,\text{exp}}$) as shown in Fig. 3. Accordingly, we consider that an additional contribution is required and that may come from the paramagnetic alignment of *R* spins, induced due to the ordering of the Fe sublattice. Further, considering the combined effect of
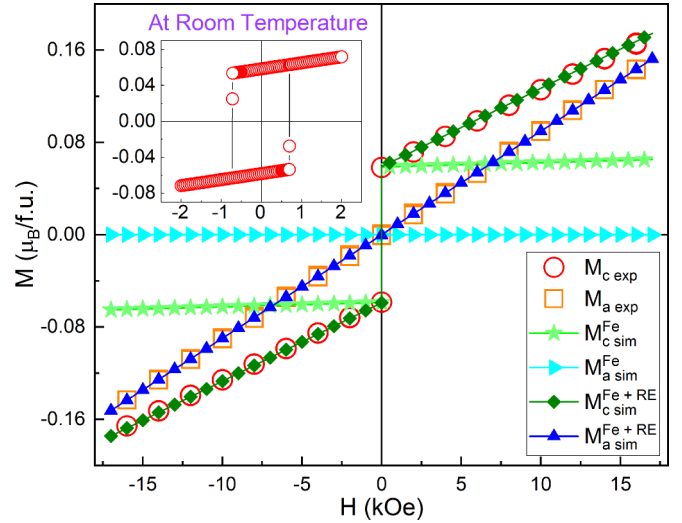

FIG. 3. Isothermal magnetization (*M*) versus magnetic field (*H*) curves measured along *a* and *c* at 300 K. The inset shows magnified view of hysteresis in *M-H* curve along *c*.

the ordered Fe sublattice and paramagnetic *R* sublattice, we simulated the magnitude of magnetization, $M_{c\,\text{sim}}^{\text{Fe}+R}$ ($M_{a\,\text{sim}}^{\text{Fe}+R}$), and matched it to $M_{c\,\text{exp}}$ ($M_{a\,\text{exp}}$) as shown in Fig. 3.

It is clear that the paramagnetic term of the *R* sublattice is essential; however, only a certain fraction, i.e., 19.8% (27.6%) of this term was needed to match the observed $M_{c\,\text{exp}}$ ($M_{a\,\text{exp}}$) at RT while computing $M_{c\,\text{sim}}^{\text{Fe}+R}$ ($M_{a\,\text{sim}}^{\text{Fe}+R}$). The details hint at the possibility of weak AFM ordering between Fe and *R* sublattice. A more detailed analysis is required to substantiate this inference.

B. Room-temperature SMR studies

In orthoferrites, the magnetic phase is influenced by both temperature and applied magnetic field. Under the application of high fields along *a*, *b*, and *c*, the spin moment configuration tends to stabilize in Γ_2, Γ_3, and Γ_4 phases, respectively (see Fig. 1). In our spin-transport studies, **H** of constant magnitude is rotated in the *ac* plane of $Ho_{0.5}Dy_{0.5}FeO_3$ single crystal. Angular dependence of $\rho_{\text{exp}}^{\text{SMR trans}}$ was measured at different specific *H* values between 350 Oe to 16 kOe. **H** was rotated in both a forward and reverse sense and the respective $\rho_{\text{exp}}^{\text{SMR trans}}$ scans, α scan, and $-\alpha$ scan were recorded. We classify our SMR studies in to two field regimes: (1) $H > H_c$ and (2) $H < H_c$.

1. $H > H_c$

We will first discuss the SMR results at high field (3–16 kOe) well above the H_c (713 Oe) [see Fig. 4(a)]. $\rho_{\text{exp}}^{\text{SMR trans}}$ varies gradually and exhibits sudden changes around $\alpha = 90°$ and 270°. A narrow hysteresis (4.5°) is seen in $\rho_{\text{exp}}^{\text{SMR trans}}$ which matches the step size of the α scan, i.e., $\Delta\alpha$. The hysteresis, which comprises a steplike sharp change in α and $-\alpha$ scans, is centered around *a* ($-a$), i.e., $\alpha = 90°$ (270°). However, the data cannot be explained solely on the basis of expected periodicity of 180° in SMR as marked by arrows in the figure. It is prudent to examine the possible contributions
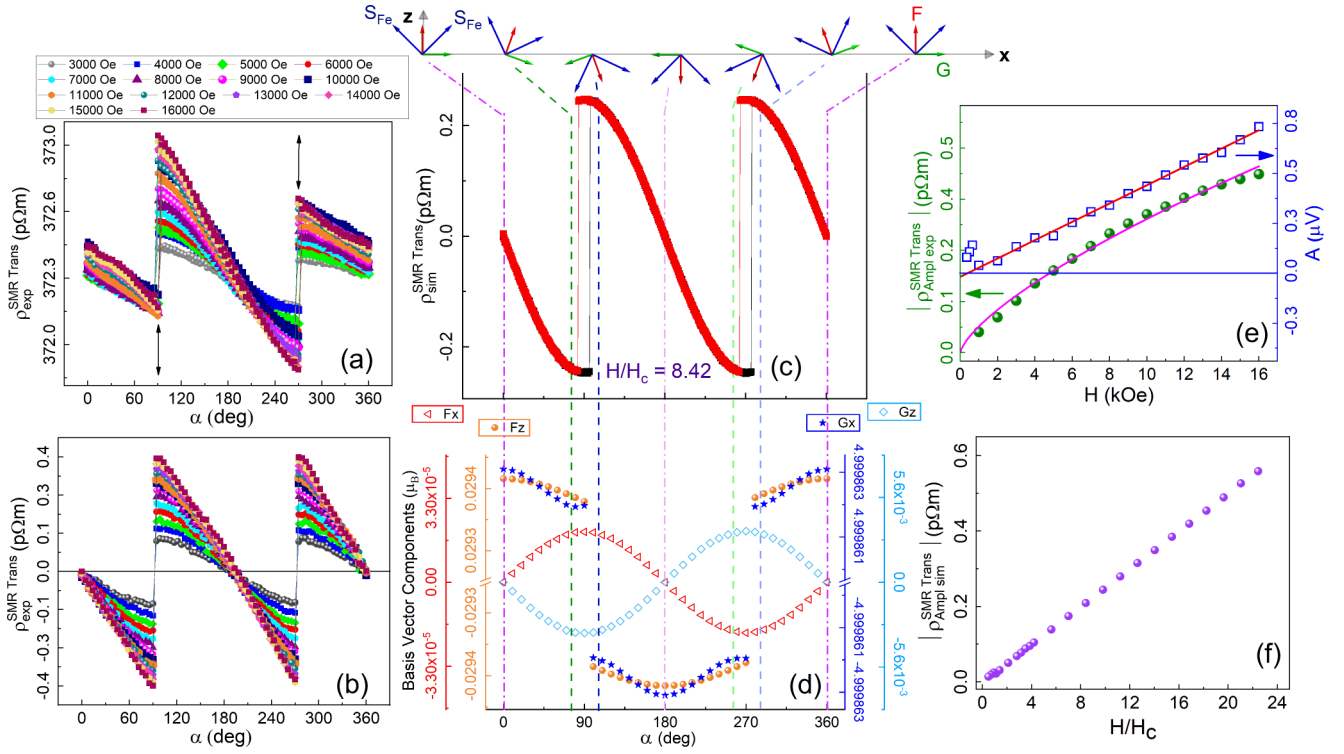
FIG. 4. Transverse SMR measured for α and $-\alpha$ scans at RT under application of various constant in-plane magnetic fields in the range of 3 kOe to 16 kOe. (a) Angular dependence of raw SMR data with asymmetry marked by black arrows. (b) Corrected SMR versus α after removal of sinusoidal contribution. Angular variation of equilibrium spin configuration (Γ_4 phase) in ac plane is computed. (c) Simulated SMR data. (d) Respective basis vector components (F_x, F_z, G_x, and G_z) versus α. (e) Field variation of extracted amplitude of sinusoidal contribution (blue squares) from raw SMR data and the amplitude of corrected SMR data (green spheres). (f) Amplitude of simulated SMR as a function of magnetic field.

in the overall signal that originates from SHAHE and OHE having periodicity of $360°$ [refer to Eq. (1)]. To estimate the SMR contribution in $\rho_{\mathrm{exp}}^{\mathrm{SMR\ trans}}$, we have removed $A \sin(\alpha + \delta)$ magnitude from the experimental curve where A and δ are the respective amplitude and phase difference of SHAHE or OHE contributions. The separated contributions of $\rho_{\mathrm{exp}}^{\mathrm{SMR\ trans}}$ and $A\sin(\alpha + \delta)$ signals are characterized by $\rho_{\mathrm{ampl\ exp}}^{\mathrm{SMR\ trans}}$ and A, respectively, and are plotted as a function of H in Fig. 4(e). The field variation of $\rho_{\mathrm{trans}}^{\mathrm{SMR\ ampl}}$ is found to be nonlinear, which is fitted with a function, cH^γ. The fit parameters c and γ are estimated as 4.68×10^{-16} and 0.71, respectively. On the other hand, the overall field variation of A is linear with a sharp discontinuity at low field (≈ 650 Oe). The high-field ($H > H_c$) contribution extracted from modulated $\rho_{\mathrm{exp}}^{\mathrm{SMR\ trans}}$ cannot be explained by SHAHE as its amplitude increases with an increase in H. On the other hand, OHE caused by OOP tilting of the sample is a likely mechanism to explain the sinusoidal contribution in $\rho_{\mathrm{exp}}^{\mathrm{SMR\ trans}}$ (refer to Appendix C).

After removal of the OHE contribution, the corrected $\rho_{\mathrm{exp}}^{\mathrm{SMR\ trans}}$ versus α curves are plotted in Fig. 4(b). The periodicity of the curves is $180°$ as expected for the typical SMR modulation. Angular variation of $\rho_{\mathrm{exp}}^{\mathrm{SMR\ trans}}$ shows continuous behavior except in the vicinity of $\boldsymbol{a}$ ($\alpha = 90°$) and $-\boldsymbol{a}$ ($\alpha = 270°$). Notably, the value $\rho_{\mathrm{exp}}^{\mathrm{SMR\ trans}}$ is zero near $\boldsymbol{c}$ ($\alpha = 0°$) and $-\boldsymbol{c}$ ($\alpha = 180°$). Our $\rho_{\mathrm{exp}}^{\mathrm{SMR\ trans}}$ data exhibits negative SMR. It has been shown that AFM Néel (basis) vector $\boldsymbol{G}$ and FM basis vector $\boldsymbol{F}$ yields negative and positive

SMR, respectively [18,19]. The observed negative SMR in $Ho_{0.5}Dy_{0.5}FeO_3$ may be due to the dominance of G over F. It is appropriate to examine if the measured signal originates from magnetostriction of $DyFeO_3$ crystal alone. For instance, a sizable magnetostriction may affect the resistance of the adjacent Pt Hall bar through the change in its dimensions or it may alter the transverse conductivity of Pt via some mechanism. In this context, a previous study by Gyorgy et al. [48], which reports comparison of angle-dependant magnetic torque and magnetostriction in the ac plane of $Sm_{0.6}Er_{0.4}FeO_3$ in a Γ_4 phase, provides useful insights. The torque was reported to change sharply (discontinuously) with sign-reversal near the a axis showing resemblance to SMR curve in our work. On the contrary, the magnetostriction curve was continuous near the a axis. Therefore, we argue that a possible parasitic magnetoresistance (MR) signal that could originate from magnetostriction would also have the same qualitative behavior, i.e., continuous variation near a axis. Since the recorded SMR curves in our work exhibit discontinuity (sharp change with sign reversal) near the a axis, we rule out the presence of parasitic MR signals (due to magnetostriction) in our recorded SMR curves.

To understand the modulation of $\rho_{\mathrm{exp}}^{\mathrm{SMR\ trans}}$ and the underlying mechanism, we first minimized $\mathcal{H}$ in Eq. (B2) using parameters listed in Table I, determined equilibrium spin configuration, included paramagnetic contribution of the R sublattice, and then computed $\rho_{\mathrm{sim}}^{\mathrm{SMR\ trans}}$ using Eq. (1). As discussed earlier, the paramagnetic alignment of the

TABLE I. Various constants and parameters used in the effective Hamiltonian for Γ_4 phase ($H = 0$ Oe) in $Ho_{0.5}Dy_{0.5}FeO_3$ system.

Exchange constants (meV)	J_c	5.2
	J_{ab}	5.1
	J_{NN}	0.2
DM vector components (meV)	α_{ab}	0.0312
	β_{ab}	0.0294
	γ_{ab}	0.0424
	α_c	0.0451
	β_c	0.1222
Anisotropy constants (meV)	K_a	−0.0055
	K_c	−0.00305
μ_{para}		10.4

R sublattice has a significant contribution in magnetization. However, in the Fe- sublattice as *G* dominates over *F* in determining the SMR, the paramagnetic contribution to SMR is found negligible compared to that in the Fe sublattice. We note that all exchange, DM, and anisotropy terms are essential in the Hamiltonian and affect the equilibrium spin configuration and computed values of SMR. As discussed in Eq. (B3), *B* in the Zeeman energy term was calculated using the experimentally measured magnetization $M_{c\,exp}$ and $M_{a\,exp}$ along *c* and *a*, respectively. This simple approach helped to simulate the hysteresis associated with α and $-\alpha$ scans which resembles our experimental result. The simulated $\rho_{sim}^{SMR\,trans}$ (α and $-\alpha$ scans) at $H/H_c = 22.5$ is shown in Fig. 4(c). A comparison of $\rho_{sim}^{SMR\,trans}$ with $\rho_{exp}^{SMR\,trans}$ data yielded the value of $\Delta\rho_1$ to be 1×10^{-10} Ωm. A schematic describing angular evolution of the spin configuration is represented at the top of the figure. Figure 4(d) shows angular variation of basis vector components (F_x, F_z, G_x, and G_z) of the spin configuration. Angular modulation of F_x and G_z is continuous while F_z and G_x show sharp changes around $\alpha = 90°$ and $\alpha = 270°$, pointing toward sudden switching between $\Gamma_4(G_x, F_z)$ and $\Gamma_4(-G_x, -F_z)$ domains. We argue that the switching and related rotational hysteresis are governed by H_c. In the α scan, both *F* and *G* vectors are confined and rotate in the *ac* plane, where they remain perpendicular to each other.

The variation of calculated $\rho_{sim\,ampl}^{SMR\,trans}$ versus H/H_c shows a linear behavior [see Fig. 4(f)]. The change in SMR amplitude can be understood in the following manner: In the absence of anisotropy, during the α scan, the $\Gamma_4(G_x, F_z)$ domain would rotate synchronously with rotating *H* and result in $-\sin(2\alpha)$ behavior of SMR with extremum value at 45°. On the other hand, in the presence of strong anisotropy, the $\Gamma_4(G_x, F_z)$ domain rotates to a small angle (yielding an increase in SMR) before it suddenly switches to the $\Gamma_4(-G_x, -F_z)$ domain (reversal in the sign of the SMR). As *H* increases, the Zeeman energy starts to dominate the anisotropy and the $\Gamma_4(G_x, F_z)$ domain rotates to a higher angle before switching to $\Gamma_4(-G_x, -F_z)$. This is a possible cause for the observed increase in the amplitude of SMR with increase in *H*. Similarly, for a fixed *H* value, if the anisotropy is weakened, then the SMR amplitude would increase.

To probe the mechanism behind the observed hysteresis in $\rho_{exp}^{SMR\,trans}$ curves, we carried out SMR measurements at vari-
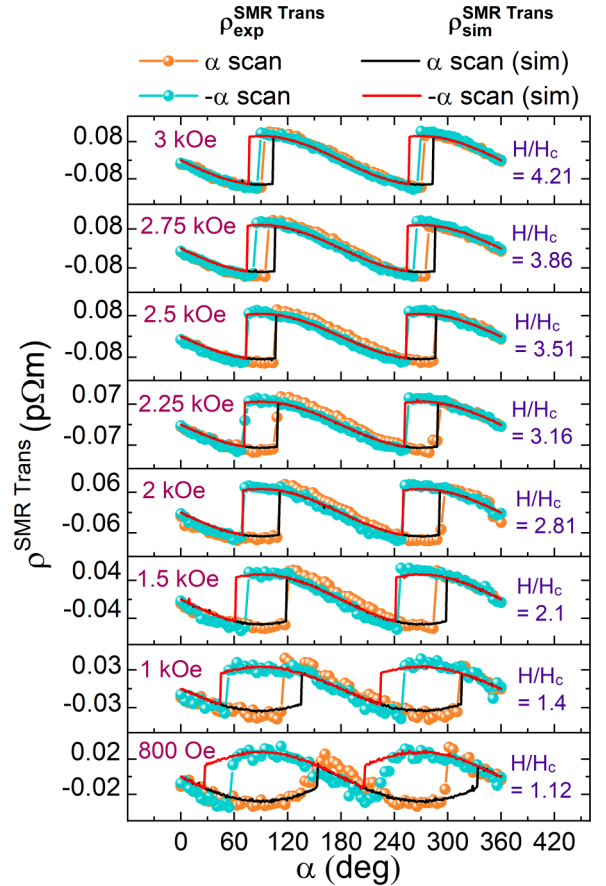

FIG. 5. Experimentally measured transverse SMR curves (α and $-\alpha$ scans) are shown for various magnetic field values (range 800 Oe to 3 kOe) just above a critical field ($H_c = 713$ Oe) and simulated SMR [α scan (sim) and $-\alpha$ scan (sim)] data at various corresponding normalized magnetic fields, denoted by H/H_c values ($H/H_c = 1.12, 1.4, 2.1, 2.81, 3.16, 3.51, 3.86$, and 4.21), are plotted.

ous fields (from 800 Oe to 3 kOe) just above H_c (713 Oe) as shown in Fig. 5. $\rho_{exp}^{SMR\,trans}$ versus α curves are highly skewed and deviate substantially from $\sin(2\alpha)$ behavior (typically observed in collinear magnets at saturation fields), indicating strong anisotropy. At 800 Oe, α and $-\alpha$ scans of $\rho_{exp}^{SMR\,trans}$ exhibit sharp changes accompanied by broad rotational hysteresis near $\alpha = 90°$ and $270°$ (Fig. 5). It is discernible that the hysteretic region decreases in size with increase in H. The hysteresis observed in the *ac* scan on $Ho_{0.5}Dy_{0.5}FeO_3$ could be interpreted as due to the first-order switching between $\Gamma_4(G_x, F_z)$ and $\Gamma_4(-G_x, -F_z)$ domains [49]. For instance, in alpha scan, $H\cos(\alpha)$ is the projection of *H* along *c*, i.e., H_c. When $\alpha > 90°$, *H* becomes negative (i.e., along $-c$) and further, when it equals to $-H_c$ (i.e., coercivity of magnetization hysteresis along *c*), the switching occurs suddenly and manifests in the sign reversal of $\rho_{exp}^{SMR\,trans}$ (a steplike feature in the SMR). It is evident that for a given value of $-H_c$, with increase in magnitude of H the width of the hysteresis decreases as seen in Fig. 5. To compare with $\rho_{exp}^{SMR\,trans}$ versus α curves, we simulated the $\rho_{sim}^{SMR\,trans}$ curves in α scan ($-\alpha$ scan) (sim) for a corresponding set of normalized magnetic fields ($H/H_c = 1.12, 1.4, 2.1, 2.81, 3.16, 3.51, 3.86$, and 4.21) as shown in Fig. 5. Reduction in the hysteretic

region with increase in H indicates the competition of Zeeman energy with the anisotropy energy.

2. $H < H_c$

In the absence of H, the Γ_4 phase possesses two possible degenerate spin configurations (domains): $\Gamma_4(G_x, F_z)$ and $\Gamma_4(-G_x, -F_z)$. Here, a single domain can be achieved by application of H higher than the coercive field H_c along c or $-c$. To obtain a single domain of $\Gamma_4(G_x, F_z)$, we applied 2 kOe field along c and subsequently reduced the field to a value (i.e., 350, 500, or 650 Oe) below H_c and then carried out the α-scan measurement. Interestingly, the angular dependence of $\rho_{exp}^{SMR\ trans}$ measured at $H = 350$, 500, and 650 Oe yielded a sinusoidal modulation with periodicity of 360° as illustrated in Fig. 6(a). Notably, the 360°-periodicity behavior does not match with the characteristic 180° periodicity of the SMR in collinear magnets. However, detailed studies are needed to understand the anomalous modulation of the observed signal. It is to be noted that $\rho_{exp}^{SMR\ trans}$ comprises three different mechanisms [see Eq. (1)]. The first two mechanisms, namely, SMR and SHAHE, are explicitly related to the spin current absorption by in-plane and OOP components of the spin moments at $Ho_{0.5}Dy_{0.5}FeO_3|Pt$ interface, respectively, whereas, the third mechanism is OHE that is solely dependent on OOP component of the H.

To examine the possible role of OHE, we carried out $\rho_{exp}^{SMR\ trans}$ measurements at $H = 350$, 500, and 650 Oe after obtaining another single domain $\Gamma_4(-G_x, -F_z)$ by employing 2 kOe field along $-c$ [refer to Fig. 6(b)]. It is discernible that the $\rho_{exp}^{SMR\ trans}$ modulations are reversed in sign (shifted by 180°) for all the field values. This result discards the possibility of OHE as an underlying mechanism. However, the contribution from SHAHE may arise due to the presence of the OOP component of the spin moments and the switching of such moments can result in the modulation of the SHAHE signal with the periodicity of 360°. The curves in Figs. 6(a) and 6(b) are fitted with $\rho_0 + A \sin(\alpha + \delta)$, where ρ_0 is the offset resistivity originating from the longitudinal component of the resistivity due to finite width of transverse leads, A is the amplitude, and δ the phase difference. The fitted amplitudes A are plotted as a function of H in Fig. 4(e) and are found to vary linearly with a distinct slope compared to that for $H > H_c$. The linear increase in amplitude with H is contrary to the general observation that high values of in-plane field tend to decrease the OOP component of the magnetization. Therefore, SMR could be a possible mechanism and it warrants further investigation.

For the two different domains $\Gamma_4(G_x, F_z)$ and $\Gamma_4(-G_x, -F_z)$, we simulated $\rho_{sim}^{SMR\ trans}$ curves in α scan ($-\alpha$ scan) (sim) for corresponding normalized magnetic fields just below the critical field (H/H_c = 0.49, 0.7, and 0.91) and compared with $\rho_{exp}^{SMR\ trans}$ versus α curves as shown in Figs. 6(a) and 6(b), respectively. In addition, the angular evolution of a spin configuration of $\Gamma_4(G_x, F_z)$ and $\Gamma_4(-G_x, -F_z)$ domains are represented by respective schematics in Fig. 6. At low H ($H < H_c$), as H rotates in the ac plane, Zeeman energy is not sufficient to initiate switching between $\Gamma_4(G_x, F_z)$ and $\Gamma_4(-G_x, -F_z)$ domains. Here, in the α scan (for either domain), both basis vectors F
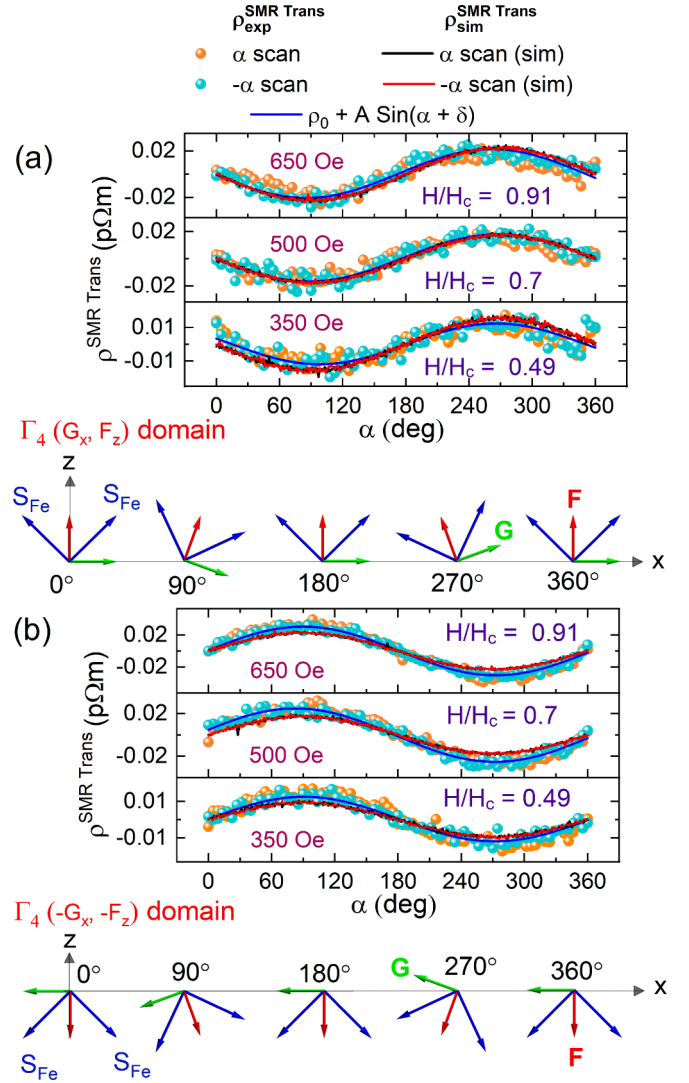

FIG. 6. Transverse SMR curves (α and $-\alpha$ scans) are plotted for various magnetic field values just below a critical field (H_c) and are denoted by corresponding normalized magnetic fields (H/H_c = 0.49, 0.7, and 0.91). (a) [or (b)] A domain $\Gamma_4(G_x, F_z)$ [or $\Gamma_4(-G_x, -F_z)$] was prepared by applying field of 2 kOe (or -2 kOe) along c and then SMR data (at room temperature) was experimentally recorded for fields (350, 500, and 650 Oe) below a critical field of $H_c = 713$ Oe. The data are fitted with sine function. Simulated SMR [α scan (sim) and $-\alpha$ scan (sim)] data are shown for corresponding H/H_c values.

and G oscillate smoothly about their mean position with 360° periodicity. It manifests in sinusoidal smooth modulation of $\rho_{sim}^{SMR\ trans}$ with periodicity of 360°. Our $\rho_{sim}^{SMR\ trans}$ curves are in good agreement with $\rho_{exp}^{SMR\ trans}$ curves [Figs. 6(a) and 6(b)]. The simulations reveal that the SMR solely accounts for the observed 360° modulation of $\rho_{exp}^{SMR\ trans}$. Here we would like to highlight that the 360° modulation of SMR at $H < H_c$, has potential in magnetic field-direction sensing devices.

Finally, we revisit and discuss key points related to the choice of ac plane for the SMR studies on $Ho_{0.5}Dy_{0.5}FeO_3|Pt$ hybrid. Typically, in $\Gamma_4(G_x, A_y, F_z)$ and $\Gamma_2(F_x, A_y, G_z)$ phases, both F and G basis vectors are prominent, where G tends to align perpendicular to H while the F favors parallel
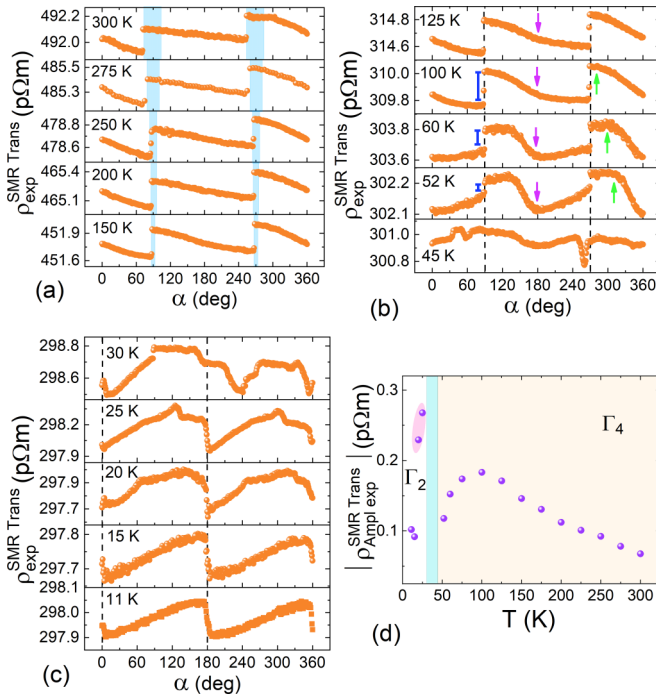
FIG. 7. Transverse SMR measured (2.4 kOe) at different temperatures in the range: (a) 300–150 K (an apparent rotational hysteresis is denoted by shaded blue region), (b) 125–4 K (the shift in peak is marked by green arrows, the bending of $\rho_{exp}^{SMR\ trans}$ near $\alpha = 180°$ is denoted using purple arrows, and the jump in $\rho_{exp}^{SMR\ trans}$ near $\alpha = 270°$ is shown by blue mark), and (c) 35–11 K (spin reorientation transition to Γ_2). (d) Temperature evolution of transverse SMR amplitude.

alignment with **H**. Therefore, for our spin-transport studies on the $\Gamma_4(G_x, A_y, F_z)$ phase at RT and investigation of the SRT to the $\Gamma_2(F_x, A_y, G_z)$ phase at lower temperature, we chose the *ac* plane of $Ho_{0.5}Dy_{0.5}FeO_3$ single crystal. Interestingly, this choice enabled us to observe a rotational hysteresis in the SMR signal, which can be associated with the switching between $\Gamma_4(G_x, F_z)$ and $\Gamma_4(-G_x, -F_z)$ domains. Here, we would like to mention that in a recent study on $DyFeO_3$ single crystal, the SMR on the *ab* plate exhibited no such hysteresis [39]. We argue that this could be possibly due to an inaccessibility of the switching between $\Gamma_4(G_x, F_z)$ and $\Gamma_4(-G_x, -F_z)$ domains in their *ab*-plane scan configuration. In the $Ho_{0.5}Dy_{0.5}FeO_3$|Pt hybrid, both **F** and **G** basis vectors stay confined in the *ac* plane during the α scan, manifesting in intriguing angular modulation of the SMR.

C. Low-temperature twofold spin reorientation transition, $\Gamma_4 \rightarrow \Gamma_1 \rightarrow \Gamma_2$

The angular dependence of $\rho_{exp}^{SMR\ trans}$ ($-\alpha$ scan) was determined by rotating **H** ($H = 2.4$ kOe) in the *ac* plane at various temperatures in the range 11–300 K [see Figs. 7(a)–7(c)]. In the absence of **H**, the high-temperature Γ_4 phase in $Ho_{0.5}Dy_{0.5}FeO_3$ persists down to 49 K before transforming to the Γ_1 phase. As discussed in the previous section, the modulation of $\rho_{exp}^{SMR\ trans}$ in the Γ_4 phase exhibits a sharp change accompanied by a rotational hysteresis while crossing *a* (see Fig. 4). The α scans were not recorded at low temperatures; however, the hysteretic region could be identified by the shift

in angle (overshoot below 90° or 270°) at which the sharp change occurred in $\rho_{exp}^{SMR\ trans}$. The width of the hysteresis, characterized by the overshoot angle, is represented by a blue-shaded region and this width is found to decrease systematically with a decrease in temperature, as shown in Fig. 7(a). As discussed in Sec. V B, the origin of hysteresis in the α-scan lies in the first-order switching of the domains [$\Gamma_4(G_x, F_z) \leftrightarrow \Gamma_4(-G_x, -F_z)$], where the angle ($\alpha$) at which the switching occurs can be estimated by the relation $H\cos\alpha = H_c$. Further, the width of the hysteresis is given by $2 \times |(90° - \alpha)|$. Notably, for all $-\alpha$ scans recorded at low temperature, H is constant (= 2.4 kOe) and it leads to $H_c \propto \cos\alpha$. Hence, the observed decrease in the width of the hysteresis can be directly related to the reduction in the magnitude of H_c. This suggests weakening of the anisotropy and favors **F** (**G**) along the *c* axis (*a* axis). Until 125 K, the amplitude of modulation, $\rho_{exp\ ampl}^{SMR\ trans}$ in the $-\alpha$ scan is determined by the magnitude of the sudden jump in $\rho_{exp}^{SMR\ trans}$ ($\rho_{exp\ jump}^{SMR\ trans}$, denoted by blue mark) around 90° and 270° ($\rho_{SMR\ trans}^{exp\ ampl} = \rho_{exp\ jump}^{SMR\ trans}/2$) [Figs. 7(a) and 7(b)]. However, below 100 K it does not hold true as the value of $\rho_{exp\ jump}^{SMR\ trans}$ tends to vanish systematically at lower temperatures until 52 K. At $T \geqslant 125$ K, the $\rho_{exp}^{SMR\ trans}$ curve peaks around 90° (270°) and in the range of 100–52 K, the peak position (shown by green arrow) shifts toward lower angles, possibly tending toward $\alpha = 45°$ (225°) [see Fig. 7(b)]. In addition, a systematic bending of the $\rho_{exp}^{SMR\ trans}$ curve (marked by a purple arrow) is seen around $\alpha = 180°$ in the same T interval. These evolutions involving $\rho_{exp\ jump}^{SMR\ trans}$, the peak shift and the bending, hint toward a gradual reduction in the skewness of $\rho_{exp}^{SMR\ trans}$ modulation tending possibly toward an ideal $\sin 2\alpha$ behavior. This reduction in the skewness of the $\rho_{exp}^{SMR\ trans}$ curve is related to a further weakening of the anisotropy. An earlier report claimed that the presence of Fe-*R* interactions in orthoferrites demands use of effective (modified) anisotropic constants [50]. As the strength of Fe-*R* interactions varies with temperature [46], the related effective anisotropic constants are temperature dependent. It is known that the strength of Fe-*R* interactions increases with decrease in the temperature and such increase in the strength of interactions could be the main mechanism responsible for the observed weakening of the anisotropy [see Figs. 7(a) and 7(b)].

In the temperature interval of 45–30 K, *H-T* phase diagram is complex involving different phases (Γ_4, Γ_1, and Γ_2) and hysteretic regions consisting of coexisting metastable phases [44] [see Figs. 7(b) and 7(c)]. $\rho_{exp}^{SMR\ trans}$ curves recorded at 45 and 30 K have multiple complex features. At temperatures below 25 K, a sharp steplike feature in the $\rho_{exp}^{SMR\ trans}$ curve is seen to occur around *c*, indicating a dominance of anisotropy favors **G** along the *c* axis in the Γ_2 phase [see Fig. 7(c)]. Thus, the SMR was found to be a useful tool to identify Γ_4 and Γ_2 phases and their respective anisotropies.

To estimate the amplitude of SMR modulation ($\rho_{exp\ ampl}^{SMR\ trans}$) at a particular temperature, we have removed the $A\sin(\alpha + \delta)$ contribution from the $\rho_{exp}^{SMR\ trans}$ curve as discussed in the previous Sec. V B. The temperature evolution of $\rho_{exp\ ampl}^{SMR\ trans}$ is plotted in Fig 7(d). In the Γ_4 phase, $\rho_{exp\ ampl}^{SMR\ trans}$ is seen to increase as the temperature is lowered to 100 K. Earlier, we have argued that as T is lowered to 100 K, the anisotropy is systematically weakened. This weakening of anisotropy

compared to the Zeeman energy (of fixed value) can cause an increase in the $|\rho_{\text{exp ampl}}^{\text{SMR trans}}|$ value (refer to the discussion in Sec. V B 1). Below 100 K, $\rho_{\text{exp ampl}}^{\text{SMR trans}}$ decreases smoothly till 52 K. As discussed in Sec. II, the paramagnetic contribution was found essential to account for the measured dc magnetization at RT. Our SMR computation includes paramagnetic contribution (refer to Sec. V A) and it is worth mentioning that its sign is opposite to that of the Fe sublattice. At RT, the paramagnetic contribution to SMR was found negligible, however, it increases as T is lowered. Below 100 K, it starts competing with that of the Fe sublattice, leading to a smooth reduction in the overall amplitude of SMR as observed in the T range, 100 K < T < 52 K. Contrary to our observations in $Ho_{0.5}Dy_{0.5}FeO_3$, the low-T paramagnetic contribution in a parent system, $DyFeO_3$ was reported to increase the net SMR as T was decreased [27]. The paramagnetic contribution, which increases with decreasing T, manifests differently in the net SMR amplitudes for $Ho_{0.5}Dy_{0.5}FeO_3$ and $DyFeO_3$, possibly due to the distinct responses of the spin configuration to the different selection of the $\boldsymbol{H}$-rotation planes, the ac plane and ab plane, respectively.

Since the T interval 45–30 K (represented by cyan color) exhibits the complex features in the $-\alpha$-scan curves, we are unable to comment on the $\rho_{\text{exp ampl}}^{\text{SMR trans}}$ variation in this range. Within the Γ_2 phase ($T \leqslant 25$ K), the variation of $\rho_{\text{exp ampl}}^{\text{SMR trans}}$ shows a drastic change between 15 and 20 K. The anomalously large values observed at 20 and 25 K are marked by pink-shaded region. The observed anomaly warrants further investigation.

VI. CONCLUSION

In this paper, we have employed SMR as a probe to examine the magnetic anisotropy and SRT in a complex 3D antiferromaget, $Ho_{0.5}Dy_{0.5}FeO_3$ possessing weak ferromagnetism (WFM). At various constant temperatures (range 300–11 K), SMR was measured on a b plate of the single crystal $Ho_{0.5}Dy_{0.5}FeO_3|Pt$ heterostructure by passing a charge current along the c direction and rotating the magnetic field ($\boldsymbol{H}$) in the ac plane (α-scan). In the RT Γ_4 phase, the basis vectors $\boldsymbol{G}$ (Néel vector) and $\boldsymbol{F}$ (WFM) lie in the ac plane. Here two competing energies, the anisotropy energy (favoring $\boldsymbol{G} \parallel \boldsymbol{a}$ and $\boldsymbol{F} \parallel \boldsymbol{c}$) and the Zeeman energy (promoting $\boldsymbol{F} \parallel \boldsymbol{H}$ and $\boldsymbol{G} \perp \boldsymbol{H}$) play a key role in the observed SMR modulation. In Γ_4 phase, a critical field $H_c = 713$ Oe was found required to overcome the anisotropy energy and cause switching between the two degenerate domains; $\Gamma_4(G_x, F_z)$ and $\Gamma_4(-G_x, -F_z)$. Transverse SMR ($\rho_{\text{exp}}^{\text{SMR trans}}$) curves ($\alpha$ and $-\alpha$ scans) recorded at $H > H_c$, exhibited a sharp change (a sign reversal) accompanied by a rotational hysteresis near the a axis. The sign-reversal and associated hysteresis are due to the first-order switching between the two domains. The hysteretic region was found to become narrower as H was increased. Further, a single domain of $\Gamma_4(G_x, F_z)$ [$\Gamma_4(-G_x, -F_z)$] was achieved using $H = 2$ (-2) kOe (here $H > H_c$) and then the SMR signal was measured at lower H (350, 500, 650 Oe), which resulted in 360°-periodicity modulation. This anomalous periodicity could be due to the smooth periodic deviation of $\boldsymbol{F}$ and $\boldsymbol{G}$ about its mean position during $\boldsymbol{H}$ rotation. To analyze

the observed SMR, we first estimated the equilibrium spin-configuration by minimizing a simple Hamiltonian, included paramagnetic contribution of R sublattice and then, computed the SMR behavior. The Hamiltonian was comprised of competing interactions acted upon Fe spins: exchange, anisotropy, Zeeman, and DM interactions. Our simulations showed close agreement with the experimentally measured SMR.

To probe SRT ($\Gamma_4 \xrightarrow{\Gamma_1} \Gamma_2$), SMR ($\alpha$ scans) under $H = 2.4$ kOe was measured at various temperatures down to 11 K. With lowering the temperature, the observed decrease in the width of the rotational hysteresis (down to 150 K) and a gradual reduction in the skewness of the $\rho_{\text{exp}}^{\text{SMR trans}}$-modulation (in the range, 100 to 52 K) point toward the weakening of the anisotropy. Our SMR data (45–30 K) reflects the complexity pertaining to various phases (Γ_4, Γ_1, and Γ_2) and phase transformations. Below 25 K, the SMR signal showed a sharp steplike feature around the c axis, indicating realization of the Γ_2 phase where $\boldsymbol{F} \parallel \boldsymbol{a}$ and $\boldsymbol{G} \parallel \boldsymbol{c}$. In summary, our studies highlight the relevance of SMR as a useful tool to track SRT as well as the anisotropy in 3D AFM and also underline the prospects of $Ho_{0.5}Dy_{0.5}FeO_3$ for use in AFM spintronic devices.

APPENDIX A: MAGNETIC PHASE REPRESENTATIONS Γ_1, Γ_2, Γ_3, AND Γ_4

Space group *Pbnm* can have various representations such as Γ_1, Γ_2, Γ_3, and Γ_4, based on the manner in which different basis vectors of the spin configuration are aligned with respect to the lattice vectors $\boldsymbol{a}$, $\boldsymbol{b}$, and $\boldsymbol{c}$. Certain basis vectors for Fe sublattices are defined in Eqs. (A1) [46]:

$$2\boldsymbol{F} = \boldsymbol{S}_1 + \boldsymbol{S}_2 + \boldsymbol{S}_3 + \boldsymbol{S}_4, \tag{A1a}$$

$$2\boldsymbol{G} = \boldsymbol{S}_1 - \boldsymbol{S}_2 + \boldsymbol{S}_3 - \boldsymbol{S}_4, \tag{A1b}$$

$$2\boldsymbol{C} = \boldsymbol{S}_1 + \boldsymbol{S}_2 - \boldsymbol{S}_3 - \boldsymbol{S}_4, \tag{A1c}$$

$$2\boldsymbol{A} = \boldsymbol{S}_1 - \boldsymbol{S}_2 - \boldsymbol{S}_3 + \boldsymbol{S}_4. \tag{A1d}$$

The basis vector $\boldsymbol{F}$ clearly represents the respective net moment in the unit cell. Other basis vectors $\boldsymbol{G}$, $\boldsymbol{C}$, and $\boldsymbol{A}$ represent the AFM behavior of orthoferrites, where generally the $\boldsymbol{G}$ basis vector is the most prominent. Spin configurations of the Fe sublattice and their representations, Γ_1, Γ_2, Γ_3, and Γ_4 are shown in Figs. 1(d)–1(g), respectively, in the main text. Notably, these four magnetic phases are represented in Bertaut's notations such as $\Gamma_1(A_x, G_y, C_z)$, $\Gamma_2(F_x, C_y, G_z)$, $\Gamma_3(C_x, F_y, A_z)$, and $\Gamma_4(G_x, A_y, F_z)$ [38]. In orthoferrites, typically at high temperatures, a $\Gamma_4(G_x, A_y, F_z)$ magnetic phase is realized [41] wherein, $\boldsymbol{G}$, $\boldsymbol{A}$, and $\boldsymbol{F}$ are aligned along $\boldsymbol{a}$, $\boldsymbol{b}$ and $\boldsymbol{c}$, respectively [see Fig. 1(g) in the main text].

APPENDIX B: ESTIMATION OF EQUILIBRIUM SPIN MOMENT CONFIGURATION

We first define the Fe spin moment (S_i) and R spin moment (S_k) in a Cartesian co-ordinate system [see Eqs. (B1a) and (B1b)]. The magnitude of Fe spin moments is denoted by $S_{Fe} = 5/2$ and that of R spin moments is $|\langle \mu_{para} \rangle|$, i.e., statistical average of effective paramagnetic moment, μ_{para}.

Our simple Hamiltonian $\mathcal{H}$ is described in Eq. (B2a), where the first two terms represent exchange interaction energy

between the nearest-neighbor Fe spins while the third term denotes exchange interaction between the next-nearest-neighbor Fe spins [see Fig. 1(b)] as discussed in Sec. II. Tilting of FeO_6 octahedra results in a local shift of oxygen atoms and in turn leads to DM interactions [fourth term in Eq. (B2a)]. A local DM interaction associated with a Fe(i)–O–Fe(j) bond can be denoted by a vector $\boldsymbol{D}_{ij}$ which follows an antisymmetric relation: $\boldsymbol{D}_{ij} = -\boldsymbol{D}_{ji}$ [47,51]. As depicted in Fig. 1(c), one basal plane consists of Fe spins S_4 and S_1 while the other plane is comprised of S_3 and S_2:

$$S_i = S_i^x \hat{x} + S_i^y \hat{y} + S_i^z \hat{z} \quad \text{such that} \quad S_{Fe} = \sqrt{(S_i^x)^2 + (S_i^y)^2 + (S_i^z)^2} \quad \text{and} \quad i = 1, 2, 3, 4, \tag{B1a}$$

$$S_k = S_k^x \hat{x} + S_k^y \hat{y} + S_k^z \hat{z} \quad \text{such that} \quad |\langle \mu_{para} \rangle| = \sqrt{(S_k^x)^2 + (S_k^y)^2 + (S_k^z)^2} \quad \text{and} \quad k = 5, 6, 7, 8, \tag{B1b}$$

$$\mathcal{H} = J_c \sum_{\langle ij \rangle}^{Fe} S_i \cdot S_j + J_{ab} \sum_{\langle ij \rangle}^{Fe} S_i \cdot S_j + J_{NN} \sum_{\langle\langle ij \rangle\rangle}^{Fe} S_i \cdot S_j$$
$$+ \sum_{\langle ij \rangle}^{Fe} \boldsymbol{D}_{ij} \cdot (S_i \times S_j) + K_a \sum_i^{Fe} (S_i^x)^2$$
$$+ K_c \sum_i^{Fe} (S_i^z)^2 - \sum_i^{Fe} \boldsymbol{B} \cdot S_i, \tag{B2a}$$

$$\mathcal{H} = 2J_c(S_1 \cdot S_2 + S_3 \cdot S_4) + 4J_{ab}(S_1 \cdot S_4 + S_2 \cdot S_3)$$
$$+ 8J_{NN}(S_1 \cdot S_3 + S_2 \cdot S_4) + 4J_{NN}(S_1 \cdot S_1 + S_2 \cdot S_2$$
$$+ S_3 \cdot S_3 + S_4 \cdot S_4) + 2\boldsymbol{D}_{14} \cdot (S_1 \times S_4)$$
$$+ 2\boldsymbol{D}'_{14} \cdot (S_1 \times S_4) + 2\boldsymbol{D}_{23} \cdot (S_2 \times S_3)$$
$$+ 2\boldsymbol{D}'_{23} \cdot (S_2 \times S_3) + 2\boldsymbol{D}_{12} \cdot (S_1 \times S_2)$$
$$+ 2\boldsymbol{D}_{34} \cdot (S_3 \times S_4) + K_a((S_1^x)^2 + (S_2^x)^2 + (S_3^x)^2$$
$$+ (S_4^x)^2) + K_c((S_1^z)^2 + (S_2^z)^2 + (S_3^z)^2 + (S_4^z)^2)$$
$$- \boldsymbol{B} \cdot (S_1 + S_2 + S_3 + S_4). \tag{B2b}$$

DM interactions in the former plane are described by the two different DM vectors, $\boldsymbol{D}_{14}(\alpha_{ab}, \beta_{ab}, -\gamma_{ab})$ and $\boldsymbol{D}'_{14}(-\alpha_{ab}, \beta_{ab}, -\gamma_{ab})$, while interactions in the latter plane are given by $\boldsymbol{D}_{23}(\alpha_{ab}, -\beta_{ab}, -\gamma_{ab})$ and $\boldsymbol{D}'_{23}(-\alpha_{ab}, -\beta_{ab}, -\gamma_{ab})$. Similarly, interplane DM interactions are denoted by $\boldsymbol{D}_{34}(-\alpha_c, \beta_c, 0)$ and $\boldsymbol{D}_{12}(\alpha_c, \beta_c, 0)$. To realize the $\Gamma_4(G_x, A_y, F_z)$ phase in the absence of magnetic field, anisotropy energy is represented by the fifth and sixth terms of Eq. (B2a), characterized by anisotropy constants, K_a and K_c, respectively (such that K_a, $K_c < 0$). The last term in Eq. (B2a) represents the Zeeman energy for Fe moments. The magnetic flux density (magnetic induction) $\boldsymbol{B}$ is defined as

$$\boldsymbol{B} = \mu_0(\boldsymbol{H} + \boldsymbol{M}_{exp}). \tag{B3}$$

Therefore, the magnitude and direction of $\boldsymbol{B}$ can be estimated with the applied magnetic field, $\boldsymbol{H}$, and experimentally measured respective magnetization, $\boldsymbol{M}_{exp}$.

Equation (B2a) can be rewritten as Eq. (B2b) after considering all relevant interactions within the nearest-neighbor and the next-nearest-neighbor Fe spins. The values of all the constants (J_c, J_{ab}, J_{NN}, α_{ab}, β_{ab}, γ_{ab}, α_c, β_c, K_a, K_c, and μ_{Para})

used in $\mathcal{H}$ [see Eq. (B2b)] are listed in Table I. It is to be noted that such constants for the parent orthoferrite $HoFeO_3$ [43] and other $RFeO_3$ [47,50] systems have been reported in previous (neutron) studies. We considered these values as reference and altered them to mimic our experimental results. Notably, the listed values for exchange interactions (i.e., J_c, J_{ab} and J_{NN}) and anisotropy constants (i.e., K_a and K_c) in Table I and the estimated magnitude of DM vectors in the present study; $|\boldsymbol{D}_{ab}|$ [i.e., $|\boldsymbol{D}_{ab}(\alpha_{ab}, \beta_{ab}, \gamma_{ab})|$] ≈ 0.06 meV and
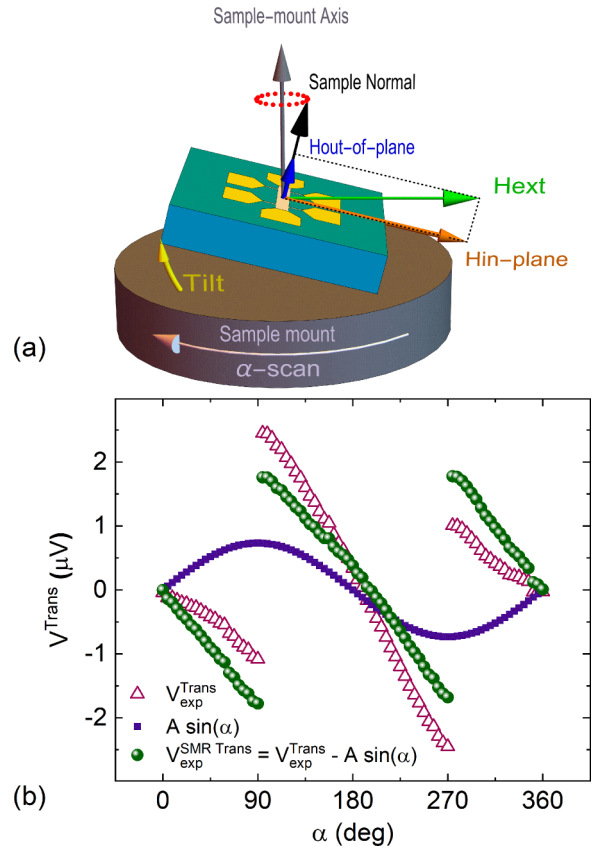

FIG. 8. (a) A schematic illustrating misalignment/tilt in the mounted sample. (b) Extraction of SMR from experimentally measured transverse voltage signal by subtracting an ordinary Hall signal.

$|\boldsymbol{D}_c|$ (i.e., $|\boldsymbol{D}_c(\alpha_c, \beta_c, 0)|) \approx 0.13$ meV are consistent with the reported values in the literature [43,47,50].

APPENDIX C: SAMPLE MISALIGNMENT-INDUCED ORDINARY HALL EFFECT

In an ideal α scan, the OHE is not present due to absence of the OOP $\boldsymbol{H}$ component. However, if the sample is not perfectly aligned on the sample mount and has a slight OOP tilt [Fig. 8(a)], then during the scan (rotation) the sample would experience the OOP $\boldsymbol{H}$ component that modulates with a period of $360°$. The outcome is the OHE signal of the same periodicity. For instance, the experimentally measured transverse voltage (V_{exp}^{trans}) at 16 kOe [Fig. 8(b)] is clearly comprised of two contributions: the SMR signal ($V_{exp}^{SMR\ Trans}$) ($180°$ periodicity) and the OHE signal ($360°$ periodicity). Figure 8(b) illustrates the procedure for extracting a symmetric SMR signal ($V_{exp}^{SMR\ trans}$) from V_{exp}^{trans} by estimating and subtracting the OHE signal. Further, as the OOP component of $\boldsymbol{H}$ scales linearly with H, the OHE signal originating from the tilt of the sample would also scale linearly with H. The extracted amplitude of OHE signal (A) versus H is plotted in Fig. 4(e). Lastly, the tilt in the sample causing OHE of magnitude $A = 0.734$ μV at $H = 16$ kOe can be estimated to be about $\approx 5°$ (ordinary Hall coefficient for 6.5-nm-thick platinum is ≈ 23.1 pΩm/T [52]).

[1] D. Hou, Z. Qiu, and E. Saitoh, Spin transport in antiferromagnetic insulators: progress and challenges, NPG Asia Mater. **11**, 35 (2019).

[2] V. Baltz, A. Manchon, M. Tsoi, T. Moriyama, T. Ono, and Y. Tserkovnyak, Antiferromagnetic spintronics, Rev. Mod. Phys. **90**, 015005 (2018).

[3] M. B. Jungfleisch, W. Zhang, and A. Hoffmann, Perspectives of antiferromagnetic spintronics, Phys. Lett. A **382**, 865 (2018).

[4] T. Jungwirth, J. Sinova, A. Manchon, X. Marti, J. Wunderlich, and C. Felser, The multiple directions of antiferromagnetic spintronics, Nat. Phys. **14**, 200 (2018).

[5] H. Yan, Z. Feng, P. Qin, X. Zhou, H. Guo, X. Wang, H. Chen, X. Zhang, H. Wu, C. Jiang *et al.*, Electric-field-controlled antiferromagnetic spintronic devices, Adv. Mater. **32**, 1905603 (2020).

[6] T. Jungwirth, X. Marti, P. Wadley, and J. Wunderlich, Antiferromagnetic spintronics, Nat. Nanotechnol. **11**, 231 (2016).

[7] P. Wadley, B. Howells, J. Železný, C. Andrews, V. Hills, R. P. Campion, V. Novák, K. Olejník, F. Maccherozzi, S. Dhesi *et al.*, Electrical switching of an antiferromagnet, Science **351**, 587 (2016).

[8] Y. Cheng, S. Yu, M. Zhu, J. Hwang, and F. Yang, Electrical Switching of Tristate Antiferromagnetic Néel Order in α-Fe$_2$O$_3$ Epitaxial Films, Phys. Rev. Lett. **124**, 027202 (2020).

[9] C. Guo, C. Wan, W. He, M. Zhao, Z. Yan, Y. Xing, X. Wang, P. Tang, Y. Liu, S. Zhang *et al.*, A nonlocal spin Hall magnetoresistance in a platinum layer deposited on a magnon junction, Nat. Electron. **3**, 304 (2020).

[10] R. Cheng, D. Xiao, and J.-G. Zhu, Antiferromagnet-based magnonic spin-transfer torque, Phys. Rev. B **98**, 020408(R) (2018).

[11] Y. Cheng, K. Chen, and S. Zhang, Giant magneto-spin-seebeck effect and magnon transfer torques in insulating spin valves, Appl. Phys. Lett. **112**, 052405 (2018).

[12] Y. Chen, E. Cogulu, D. Roy, J. Ding, J. B. Mohammadi, P. G. Kotula, N. A. Missert, M. Wu, and A. D. Kent, Spin transport in an insulating ferrimagnetic-antiferromagnetic-ferrimagnetic trilayer as a function of temperature, AIP Adv. **9**, 105319 (2019).

[13] C. Y. Guo, C. H. Wan, X. Wang, C. Fang, P. Tang, W. J. Kong, M. K. Zhao, L. N. Jiang, B. S. Tao, G. Q. Yu, and X. F. Han, Magnon valves based on YIG| NiO|YIG all-insulating magnon junctions, Phys. Rev. B **98**, 134426 (2018).

[14] D. Hou, Z. Qiu, J. Barker, K. Sato, K. Yamamoto, S. Vélez, J. M. Gomez-Perez, L. E. Hueso, F. Casanova, and E. Saitoh, Tunable Sign Change of Spin Hall Magnetoresistance in Pt|NiO|YIG Structures, Phys. Rev. Lett. **118**, 147202 (2017).

[15] H. Wang, D. Hou, Z. Qiu, T. Kikkawa, E. Saitoh, and X. Jin, Antiferromagnetic anisotropy determination by spin Hall magnetoresistance, J. Appl. Phys. **122**, 083907 (2017).

[16] A. Aqeel, N. Vlietstra, A. Roy, M. Mostovoy, B. J. van Wees, and T. T. M. Palstra, Electrical detection of spiral spin structures in Pt|Cu$_2$OSeO$_3$ heterostructures, Phys. Rev. B **94**, 134418 (2016).

[17] R. Lebrun, A. Ross, O. Gomonay, S. A. Bender, L. Baldrati, F. Kronast, A. Qaiumzadeh, J. Sinova, A. Brataas, R. Duine *et al.*, Anisotropies and magnetic phase transitions in insulating antiferromagnets determined by a spin-Hall magnetoresistance probe, Commun. Phys. **2**, 50 (2019).

[18] J. Fischer, O. Gomonay, R. Schlitz, K. Ganzhorn, N. Vlietstra, M. Althammer, H. Huebl, M. Opel, R. Gross, S. T. B. Goennenwein, and S. Geprägs, Spin Hall magnetoresistance in antiferromagnet|heavy-metal heterostructures, Phys. Rev. B **97**, 014417 (2018).

[19] S. Geprägs, M. Opel, J. Fischer, O. Gomonay, P. Schwenke, M. Althammer, H. Huebl, and R. Gross, Spin Hall magnetoresistance in antiferromagnetic insulators, J. Appl. Phys. **127**, 243902 (2020).

[20] H. Nakayama, M. Althammer, Y.-T. Chen, K. Uchida, Y. Kajiwara, D. Kikuchi, T. Ohtani, S. Geprägs, M. Opel, S. Takahashi, R. Gross, G. E. W. Bauer, S. T. B. Goennenwein, and E. Saitoh, Spin Hall Magnetoresistance Induced by a Nonequilibrium Proximity Effect, Phys. Rev. Lett. **110**, 206601 (2013).

[21] Y.-T. Chen, S. Takahashi, H. Nakayama, M. Althammer, S. T. B. Goennenwein, E. Saitoh, and G. E. W. Bauer, Theory of spin Hall magnetoresistance, Phys. Rev. B **87**, 144411 (2013).

[22] Y.-T. Chen, S. Takahashi, H. Nakayama, M. Althammer, S. T. Goennenwein, E. Saitoh, and G. E. Bauer, Theory of spin Hall magnetoresistance (SMR) and related phenomena, J. Phys.: Condens. Matter **28**, 103004 (2016).

[23] T. Kato, Y. Ohnuma, and M. Matsuo, Microscopic theory of spin Hall magnetoresistance, Phys. Rev. B **102**, 094437 (2020).

[24] X.-P. Zhang, F. S. Bergeret, and V. N. Golovach, Theory of spin Hall magnetoresistance from a microscopic perspective, Nano Lett. **19**, 6330 (2019).

[25] D. A. Reiss, T. Kampfrath, and P. W. Brouwer, Theory of spin-Hall magnetoresistance in the ac terahertz regime, Phys. Rev. B **104**, 024415 (2021).

[26] K. Mallick, A. A. Wagh, A. Ionescu, C. H. W. Barnes, and P. S. Anil Kumar, Role of spin mixing conductance in determining thermal spin pumping near the ferromagnetic phase transition in EuO_{1-x} and La_2NiMnO_6, Phys. Rev. B **100**, 224403 (2019).

[27] G. R. Hoogeboom, G.-Jan N. Sint Nicolaas, A. Alexander, O. Kuschel, J. Wollschläger, I. Ennen, B. J. van Wees, and T. Kuschel, Role of NiO in the nonlocal spin transport through thin NiO films on $Y_3Fe_5O_{12}$, Phys. Rev. B **103**, 144406 (2021).

[28] W. Lin and C. L. Chien, Electrical Detection of Spin Back-flow from an Antiferromagnetic Insulator|$Y_3Fe_5O_{12}$ Interface, Phys. Rev. Lett. **118**, 067202 (2017).

[29] T. Shang, Q. Zhan, H. Yang, Z. Zuo, Y. Xie, L. Liu, S. Zhang, Y. Zhang, H. Li, B. Wang *et al.*, Effect of NiO inserted layer on spin-Hall magnetoresistance in Pt| NiO|YIG heterostructures, Appl. Phys. Lett. **109**, 032410 (2016).

[30] J.-S. Zhou, L. G. Marshall, Z.-Y. Li, X. Li, and J.-M. He, Weak ferromagnetism in perovskite oxides, Phys. Rev. B **102**, 104420 (2020).

[31] Z. Zhou, L. Guo, H. Yang, Q. Liu, and F. Ye, Hydrothermal synthesis and magnetic properties of multiferroic rare-earth orthoferrites, J. Alloys Compd. **583**, 21 (2014).

[32] Y. Tokunaga, Y. Taguchi, T. Arima, and Y. Tokura, Magnetic Biasing of a Ferroelectric Hysteresis Loop in a Multiferroic Orthoferrite, Phys. Rev. Lett. **112**, 037203 (2014).

[33] Y. Tokunaga, S. Iguchi, T. Arima, and Y. Tokura, Magnetic-Field-Induced Ferroelectric State in $DyFeO_3$, Phys. Rev. Lett. **101**, 097205 (2008).

[34] T. Chakraborty, T. Sarkar, P. A. Kumar, and S. Elizabeth, High temperature negative magnetization, spin reorientation and their suppression with magnetic field in $ErFe_{0.55}Mn_{0.45}O_3$ single crystal, J. Alloys Compd. **767**, 392 (2018).

[35] T. Hajiri, L. Baldrati, R. Lebrun, M. Filianina, A. Ross, N. Tanahashi, M. Kuroda, W. Gan, T. Menteş, F. Genuzio *et al.*, Spin structure and spin Hall magnetoresistance of epitaxial thin films of the insulating non-collinear antiferromagnet $SmFeO_3$, J. Phys.: Condens. Matter **31**, 445804 (2019).

[36] K. P. Belov, A. K. Zvezdin, A. M. Kadomtseva, and R. Levitin, Spin-reorientation transitions in rare-earth magnets, Sov. Phys. Usp. **19**, 574 (1976).

[37] S. Becker, A. Ross, R. Lebrun, L. Baldrati, S. Ding, F. Schreiber, F. Maccherozzi, D. Backes, M. Kläui, and G. Jakob, Electrical detection of the spin reorientation transition in antiferromagnetic $TmFeO_3$ thin films by spin Hall magnetoresistance, Phys. Rev. B **103**, 024423 (2021).

[38] E. Bertaut, Representation analysis of magnetic structures, Acta Cryst. A **24**, 217 (1968).

[39] G. R. Hoogeboom, T. Kuschel, G. E. W. Bauer, M. V. Mostovoy, A. V. Kimel, and B. J. van Wees, Magnetic or-

der of Dy^{3+} and Fe^{3+} moments in antiferromagnetic $DyFeO_3$ probed by spin Hall magnetoresistance and spin Seebeck effect, Phys. Rev. B **103**, 134406 (2021).

[40] M. H. Mohammed, J. Horvat, Z. Cheng, S. Cao, E. Li, and R. Li, Magnetic interaction between Pr^{3+} and Dy^{3+} spins and their spin transition induced by magnetic field in a $Dy_{0.5}Pr_{0.5}FeO_3$ single crystal, J. Phys. Chem. C **123**, 30584 (2019).

[41] E. Li, Z. Feng, B. Kang, J. Zhang, W. Ren, and S. Cao, Spin switching in single crystal $PrFeO_3$ and spin configuration diagram of rare earth orthoferrites, J. Alloys Compd. **811**, 152043 (2019).

[42] M. Shao, S. Cao, Y. Wang, S. Yuan, B. Kang, J. Zhang, A. Wu, and J. Xu, Single crystal growth, magnetic properties and Schottky anomaly of $HoFeO_3$ orthoferrite, J. Cryst. Growth **318**, 947 (2011).

[43] A. Ovsyanikov, I. Zobkalo, W. Schmidt, S. Barilo, S. Guretskii, and V. Hutanu, Neutron inelastic scattering study of rare-earth orthoferrite HoFeO3, J. Magn. Magn. Mater. **507**, 166855 (2020).

[44] T. Chakraborty and S. Elizabeth, Two fold spin reorientation and field induced phase transition in $Ho_{0.5}Dy_{0.5}FeO_3$ single crystal, J. Magn. Magn. Mater. **462**, 78 (2018).

[45] I. Mikami, Paramagnetic behavior of rare-earth ions in some orthoferrites, J. Phys. Soc. Jpn. **34**, 338 (1973).

[46] T. Yamaguchi, Theory of spin reorientation in rare-earth orthochromites and orthoferrites, J. Phys. Chem. Solids **35**, 479 (1974).

[47] K. Park, H. Sim, J. C. Leiner, Y. Yoshida, J. Jeong, S.-i. Yano, J. Gardner, P. Bourges, M. Klicpera, V. Sechovský *et al.*, Low-energy spin dynamics of orthoferrites $AFeO_3$ (A = Y, La, Bi), J. Phys.: Condens. Matter **30**, 235802 (2018).

[48] E. M. Gyorgy, L. G. Van Uitert, E. C. Heisler, Jr., and W. G. Grodkiewicz, Magnetostriction of some rare-earth orthoferrites, J. Appl. Phys. **42**, 482 (1971).

[49] Y. B. Bazaliy, L. T. Tsymbal, G. N. Kakazei, A. I. Izotov, and P. E. Wigen, Spin-reorientation in $ErFeO_3$: Zero-field transitions, three-dimensional phase diagram, and anisotropy of erbium magnetism, Phys. Rev. B **69**, 104429 (2004).

[50] S. E. Nikitin, L. S. Wu, A. S. Sefat, K. A. Shaykhutdinov, Z. Lu, S. Meng, E. V. Pomjakushina, K. Conder, G. Ehlers, M. D. Lumsden, A. I. Kolesnikov, S. Barilo, S. A. Guretskii, D. S. Inosov, and A. Podlesnyak, Decoupled spin dynamics in the rare-earth orthoferrite $YbFeO_3$: Evolution of magnetic excitations through the spin-reorientation transition, Phys. Rev. B **98**, 064424 (2018).

[51] M. Mochizuki and N. Furukawa, Microscopic model and phase diagrams of the multiferroic perovskite manganites, Phys. Rev. B **80**, 134416 (2009).

[52] S. Meyer, R. Schlitz, S. Geprägs, M. Opel, H. Huebl, R. Gross, and S. T. Goennenwein, Anomalous Hall effect in YIG|*Pt* bilayers, Appl. Phys. Lett. **106**, 132402 (2015).